Chapter 3

BREAKING INTO PIECES: IN-SITU FRACTURE EXPERIMENTS PERFORMED ON A GLASS-CERAMIC

Sections of this chapter will be published in a forthcoming publication: **Gorske, S.F.**, Shanks, K., Voorhees, P., Faber, K.T. "3D brittle crack paths in an alkali-aluminosilicate glass-ceramic visualized in-situ using synchrotron X-rays and stable fracture geometry." In preparation.

3.1 Introduction

Glass-ceramics are an ideal class of materials on which to test the proposed experimental setup. The isotropic matrix, usually a silicate or aluminosilicate, resembles the previous DCDC tests on glasses and idealized models, while the presence of second-phase crystals can disrupt the strict Mode I crack of the ideal sample by introducing residual stresses and anisotropic lattices that can serve to deflect, attract, or arrest the crack's motion [1].

Glass-ceramics have found increasing use in applications requiring materials with greater strength and fracture toughness than typical glasses. For many glass-ceramics, the second-phase particles, which have different elastic moduli and fracture toughnesses than the surrounding matrix, create residual stress fields within the isotropic matrix as a result of thermal mismatch between the two phases. The first processing step is to bring the material past its melting temperature, then to cool it to and hold it at a temperature below the melting point but much higher than that which it is used at. Here, nucleation of the second phase particles is induced, and those particles grow through Ostwald ripening [2]. At temperatures under the liquidus but greater than the glass transition temperature, the material that will become the matrix is still soft, allowing the particles to grow without the hindrance of existing interfaces. Upon cooling, however, the difference in thermal expansion parameters between the matrix and the grains results in residual stress being distributed within the grains and the matrix [3–6].

Many second-phase crystals have larger thermal expansion coefficients than a typical glass, so if the matrix did not contain grains but rather empty cavities, those spaces would not shrink as fast as isolated trevorite crystals. In order for the grains to remain bonded to the

matrix, tensile stress needs to develop within the grains, while the matrix experiences tensile radial stresses and compressive tangential stresses. As a result, when a crack grows into the volume surrounding a particle, it will be deflected away from the particles, serving as an effective toughening mechanism [3,5]. In contrast, a crystalline phase with a lower thermal expansion coefficient than the matrix has less resistance to cracking and will attract the crack. Additionally, factors such as particle shape [5], density [1], and size [7] affect the overall toughening effect, all of which may be tuned through careful selection of precursor materials, which usually are a number of different oxide minerals [2].

Such crack deflections and reorientations are of interest to modelers of real materials. Many materials are composites and include particles, fibers, or other second-phase materials, and both composites and single-phase materials often have interior flaws which impact performance, and reliability. Understanding the paths cracks take between, around, and through particles, the locations of fastest and slowest growth, where the crack first appears, and any places where the crack might stop propagating, all under real loading conditions, will help modelers and developers of brittle materials to improve the understanding and implementation of materials for real-world applications.

For this first set of experiments, a system with a few measurable properties influencing crack growth was sought, both in order to reduce the number of variables that must be accounted for when creating a model, and to ensure the DCDC geometry would produce cracks as expected. Thus, a glass-ceramic with a cubic phase was chosen to minimize anisotropy and high aspect ratios in the crystals, with a goal to achieve equiaxed particles with minimum 10 μm diameter so they could be resolved in all directions using μ-CT. A system developed by the Pacific Northwest National Laboratory (PNNL) to mimic high-level waste satisfied these conditions, with cubic particles of trevorite, $NiFe_2O_4$, space group 227, in the spinel system, suspended in an alkali-aluminosilicate glassy matrix [8]. The system will be henceforth termed the trevorite glass-ceramic (TGC) in this thesis.

3.2 Materials and Methods

3.2.1 Materials

The heat-treated glassy precursors to the TGC were obtained from PNNL, including samples of Ni-1.5 and OL-02 oxide mixtures as described by Lonergan, et al. [8]. Shards of the glass mixtures in a ratio of 7 parts Ni-1.5 to 1 part OL-02 were mixed together, resulting in a material containing thirty different precursor oxides. Oxides present in greater than 1 wt% were: SiO_2 (39.69%), Na_2O (17.25%), Fe_2O_3 (14.90%), Al_2O_3 (8.45%), B_2O_3 (7.68%), ZrO_2 (3.90%), Li_2O (2.21%), NiO (1.32%), and MnO (1.07%), which together made up 96.47% of the material's weight. The shards were then placed in a 10 mL platinum crucible inside a CM Rapid Temp box furnace. The furnace was taken up to 1200 °C and held for 24 h, then lowered to 900 °C and held for 44 h before quenching to room temperature. Both temperature ramps were performed at a rate of 10 °C/min. The TGC was then removed from the crucible and examined for average grain size using optical microscopy. The grains generally had polyhedral shapes with defined facets (Figure 3.1a).

The visible grain areas were extracted by thresholding the images and analyzing the resultant particles with ImageJ, and the diameters were calculated with a square basis as an assumption. To verify that the grains were large enough for good-quality FF-HEDM and μ-CT data, for which a 10 μm diameter was the goal, an estimate for the average diameter was calculated based on Cuzzi and Olson's work [9]; while the equations used were designed for spheres, the grains present generally appeared to be equiaxed and thus were deemed acceptable to use. When using an estimate for monodispersed grains, the estimated diameter was 20.3 μm, while when using Cuzzi and Olson's inverted histogram method, which is weighted less by the large grains presenting with diameters of around 40 μm, the estimated average diameter was 14.2 μm.

The TGC samples were cut using a Buehler Isomet 5000 saw into dimensions of approximately 1.4 mm x 1.4 mm x 14 mm, within a tolerance of 0.03 mm. The bars were lightly polished on a Buehler Ecomet 3 polisher using 1200-grit silicon carbide paper to remove any irregularities from the saw, and the edges on the short faces, which would come into contact with the platens, were chamfered to remove any burrs on the corners. The hole for the DCDC geometry was then lasered into two of the opposing long faces for each sample until the holes from both sides connected. The inner diameter of the intersecting cones was

around 85 μm in diameter while the outer diameter on the sample faces was about 430 μm for an average hole diameter of around 250 μm.

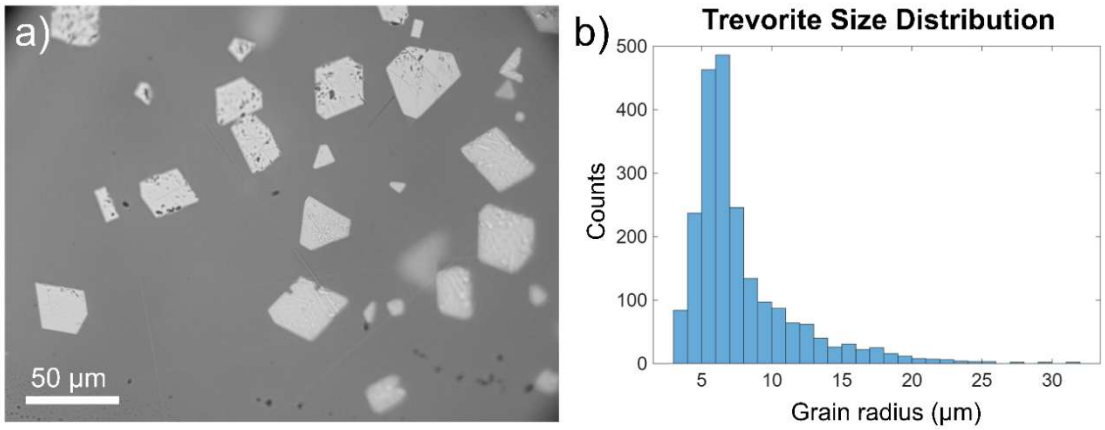

Figure 3.1: a) Optical micrograph of the polished trevorite glass-ceramic (TGC), showing faceted trevorite grains. b) Histogram of trevorite radii, as obtained from μ-CT, with mean 7.84 ± 3.83 μm.

3.2.2 Methods

Synchrotron experiments were performed at the Cornell High Energy Synchrotron Source at the ID3A Forming and Shaping Technology (FAST) beamline. A silicon (111) double-crystal monochromator was used to isolate 23.22 keV X-rays, with bandwidth $\Delta E/E = 0.002$, from the upstream undulator beam.

3.2.2.1 Loading

Compression testing was performed using the second-generation Rotational and Axial Motion System (RAMS2) [10]. The samples were loaded and centered in between hardened steel platens with 3 mm radius. Each sample's verticality was checked using live radiography and adjusted until it did not tilt in any direction. The entirety of the sample was able to be viewed by moving the load frame, allowing both the top and bottom cracks to be analyzed.

Loading was performed using displacement control. The loading direction was in the positive y direction when moving downward, such that the top of the sample was located at more negative values of y. The load cell was lowered in manual steps of fractions of a micron while watching a live radiograph of the current location of the crack front. When extension was noticed, the load cell was moved away until the load on the sample had decreased by

about 50 N. The displacement at that point was recorded and held during the following rotations and scans.

3.2.2.2 FF-HEDM

The FF-HEDM data were collected on two Dexela 2923 detectors located 0.576 m downstream of the sample. The detector distances and tilts were initially calibrated using an amorphous ceria sample, followed by a finer calibration using a polycrystalline ruby sample consisting of three strain-free grains of known orientation and location.

The beam size was set to a height of 25 μm and a width of 2.25 mm. A single 0.203 mm aluminum attenuator was inserted before the beam reached the sample to minimize detector pixel saturation. For each scan, 1440 frames were collected over a rotation from ω=0°-360° with an acquisition time of 0.25 s and a rotation step size $\Delta\omega$ of 0.25°. Scans were spaced 25 μm apart in the loading direction y.

Reconstruction of the results was performed using the HEXRD framework [11,12]. During initial reconstruction, summing all frames over 2θ produced a diffraction intensity pattern with strong peaks matching the expected material trevorite, with a strained average lattice parameter of 8.38 Å. An unstrained lattice parameter of 8.36 Å was used to calculate strain, following calculations presented in Section 3.3.1. Signals from the {111}, {220}, {311}, {222}, {400}, {422}, {333}, {511}, and {440} peaks were present with sufficient intensity to be used for reconstruction. Diffraction spots corresponding to rings in 2θ for the orientations {220}, {222}, and {400} were used for seeding of grain orientations. After initial reconstruction, grains with a goodness-of-fit parameter $\chi^2 < 0.001$ and a completeness > 0.8 were retained for further analysis.

Stress tensors were calculated from the strain tensors using the single-crystal elastic components of the stiffness tensor: C_{11} = 273.1 GPa, C_{12} = 160.7 GPa, C_{44} = 82.3 GPa [13].

3.2.2.3 μ-CT

μ-CT images were collected on a scintillator-coupled Retiga 4000DC detector, located 20.9 μm away from the sample, where the phase contrast was maximized. The beam size was set to a height of 1 mm and a width of 2.25 mm. A total of 720 images over a rotation

angle of ω=0°-180° were acquired for each scan, with a rotation angle step size $\Delta\omega$ of 0.25° and an acquisition time of 1 s per image. Scans were spaced 0.8 mm apart in the loading direction *y*.

Reconstruction was performed using the CHESS Analysis Pipeline (CHAP) tomography package [14]. The final reconstructed data had voxel sizes of 1.48 x 1.48 x 1.48 μm3 and the locations in real space were recorded for registration.

3.2.2.3.1 Image Processing for Crack Detection

The crack measured only a few μm, and therefore only a few 2D pixels, in width at its maximum, and narrowed further the deeper it extended into the sample (Figure 3.2a,b). Eventually, it became narrower than the tomographic resolution, but the phase change at the interface still resulted in a change in X-ray absorption and was detected as a narrow, bright region due to fringing at the surfaces (Figure 3.2c). The narrowness of the crack meant that it could be difficult to distinguish from background noise in many regions (Figure 3.2b,c), and a custom image processing method was constructed to locate and measure the crack.

First, reconstruction artifacts, which presented as vertical lines, were removed by opening the image with a tall rectangular structural element, then the opened image was subtracted from the original in a top hat procedure (Figure 3.2d). Next, the trevorite grains were identified by thresholding the image; grains had intensities greater than 14% of the maximum image intensity (Figure 3.2e).

A modified median filter was then applied. First, the grain locations were replaced with random noise in the full image so the true background could be smoothed without interference from the bright grains. Opened and dilated versions of the images were created using a 3x3x3 cubic structural element and averaged to remove both dark and bright noise. Most of the denoised image, excepting the regions around the hole and the crack, was then treated with a 11x11x5 median filter to further smooth the matrix background. In the region of the crack, defined as all those voxels directly above or below the hole, three types of voxel were identified: background, dark crack (wider), and bright crack (narrow). All voxels were characterized by their mean value in a 1x1x5 volume centered around the voxel of interest to strengthen the crack signal, which persists in subsequent slices, as well as their median values in 5x5x5 and 7x7x5 centered volumes. As the volumes increase in size around a crack point, both the number of background voxels and crack voxels should increase, but the

former will increase faster; thus increasing thresholds (5.6%, 5.6%, 6.3% of the maximum intensity, respectively) were set for each volume that a point had to meet to qualify as a crack point. In contrast, a true background voxel might be below the threshold, and a larger volume will also increase the median value at that point, but fewer true crack points will be included since that data point will be more isolated compared to a group of crack points close to one another. Thus one threshold might be met, but the median values of the larger volumes near the average value of the background increase faster than in a volume including many crack points. The bright regions of the crack were identified similarly, although voxels and regions needed to be above the thresholds (7.7%, 7.7%, 7.0% of the maximum intensity, respectively) rather than below. Identified dark crack points were then set to the mean value of the 1x1x5 volume, decreased in intensity by 25%; bright points were similarly replaced then increased in intensity by 20%. All other points were set to the median value of a centered 11x11x5 volume to smooth out noisy signals. The previously suppressed grains were then added back in. Contrast was then enhanced for the top and bottom 1% of pixel values and normalized over the entire stack (Figure 3.2f).

Still, some noisiness remained after this pass. To remove it, the 2D binary images representing the potential locations of the crack were divided into their connected components. Shape filtering was applied to the binary images, first requiring the retained components to have a certain size. Additionally a certain amount of non-sphericity was required, as the crack was roughly linear, while small clusters of noise were more isolated and therefore spherical. A final requirement was for the long axis of the elliptical shape containing the component to be directed along an angle within some bound of the average crack orientation; the bounding value decreased as the crack progressed deeper into the sample and became more linear [15,16]. Finally, a stack of 100 slices was summed along the direction of crack growth y, revealing the crack shape more fully, and for each image, pixels recorded as belonging to the crack in more than 12.5% of the other images were retained (Figure 3.2g,h). The points closest to the edges of the sample for each depth were then recorded to trace the outline of the crack front, since in the sample interior, the detected crack was often broken up into small sections due to proximity to grains that it jumped over, through, or around, leading to an inconsistent front appearance. Any points belonging to a slice with fewer than 100 total hits (0.005% area) were not included in the crack front trace

due to remaining noise becoming stronger than the crack signal such that the true edges were difficult to discern. The crack edge points from the last five slices on either side were then used to connect a parabolic estimate for the crack front, which was expected to be curved [17]; the deepest point was then used as the value for crack length. Positive error was calculated as the difference between the parabolic depth and the deepest slice initially found, including those with fewer than 100 hits and averaged 52 μm. Negative error was the difference between the parabolic depth and the final confident edge point and averaged 15 μm.

3.2.2.3.2 Image Processing for Grain Analysis

The thresholded, binary images of the grains were retained after they were extracted from the structurally-filtered tomography images. A watershed algorithm was applied to separate grains which were clustered together after thresholding. ImageJ's 3D object counter was used on a sample volume under no load to better estimate grain sizes; after filtering out identified objects with a volume below 25 voxels^3 (radius of less than 3 μm), the average grain radius was found to be 7.84 ± 3.83 μm, in line with the original calculated diameter of 14-20 μm (Figure 3.1b). The number density of grains present was about 15,000 grains/mm^3, with a volume density of 4.1%.

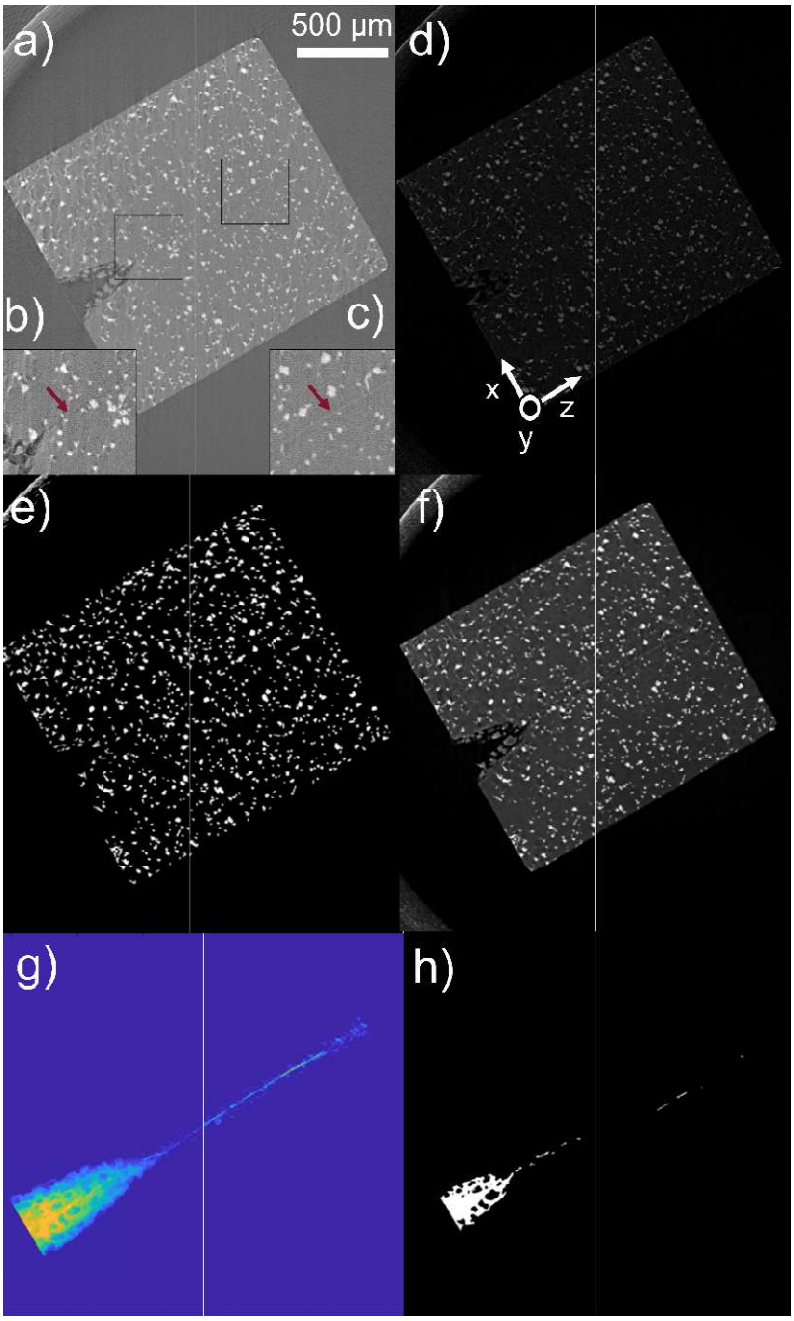

Figure 3.2: Steps in the image processing framework used to find the crack, on two sample locations, close to the hole and far. a) Reconstructed tomography slices showing b) the visible crack (dark line indicated by maroon arrow) and c) the crack when it was narrower than the tomographic resolution (bright line indicated by maroon arrow). d) Top hat image after opening with a rectangular structural element. e) Thresholded grains. f) Modified 3D median filter. g) Heat map showing relative frequency a location was marked as a crack point over 100 subsequent slices. h) Final crack points.

3.3 Results and Discussion

3.3.1 Tomography

3.3.1.1 Crack Extension

Initial pop-in of the crack was observed on both sides of the TGC sample at -498 N (Figure 3.3a). The top crack pop-in length was 0.691 mm, while the bottom side had a length of 0.655 mm. The bottom crack then extended further to 0.916 mm at a load of -523 N, while the top crack did not extend. Both sides then extended at -624 N, to 1.06 mm on the bottom and 1.02 mm on the top (Figure 3.3b). A final extension was observed at -690 N. The top of the crack extended to 1.45 mm and the bottom crack was initially estimated to extend to around 1.6 mm, but further extension occurred during the tomography scan, despite the load having been lowered to -650 N. While the bottom crack did narrow around the expected depth, it widened again a few tens of microns deeper and was detected to a depth of 2.11 mm (Figure 3.3c). Incidentally, tomography analysis revealed that during the scan, starting at around a depth of 1.6 mm and continuing to the bottom of the sample, part of one sample side had sheared off, reducing the local load-bearing area and increasing the local applied stress, which may have contributed to the crack's resumed growth. The sheared-off shard was not flat; while it was not found afterward, the remaining sample continued to taper inward toward the bottom face, causing the reduction in area to increase with sample depth, and therefore also increasing the applied load with depth. Immediately after the tomography scan at that load, the sample failed fully, which likely indicates that the bottom crack had reached an unstable point after the shearing event, as in some volume, the load distributed over the shrunken area would have exceeded that necessary to propagate the crack fully through the sample.

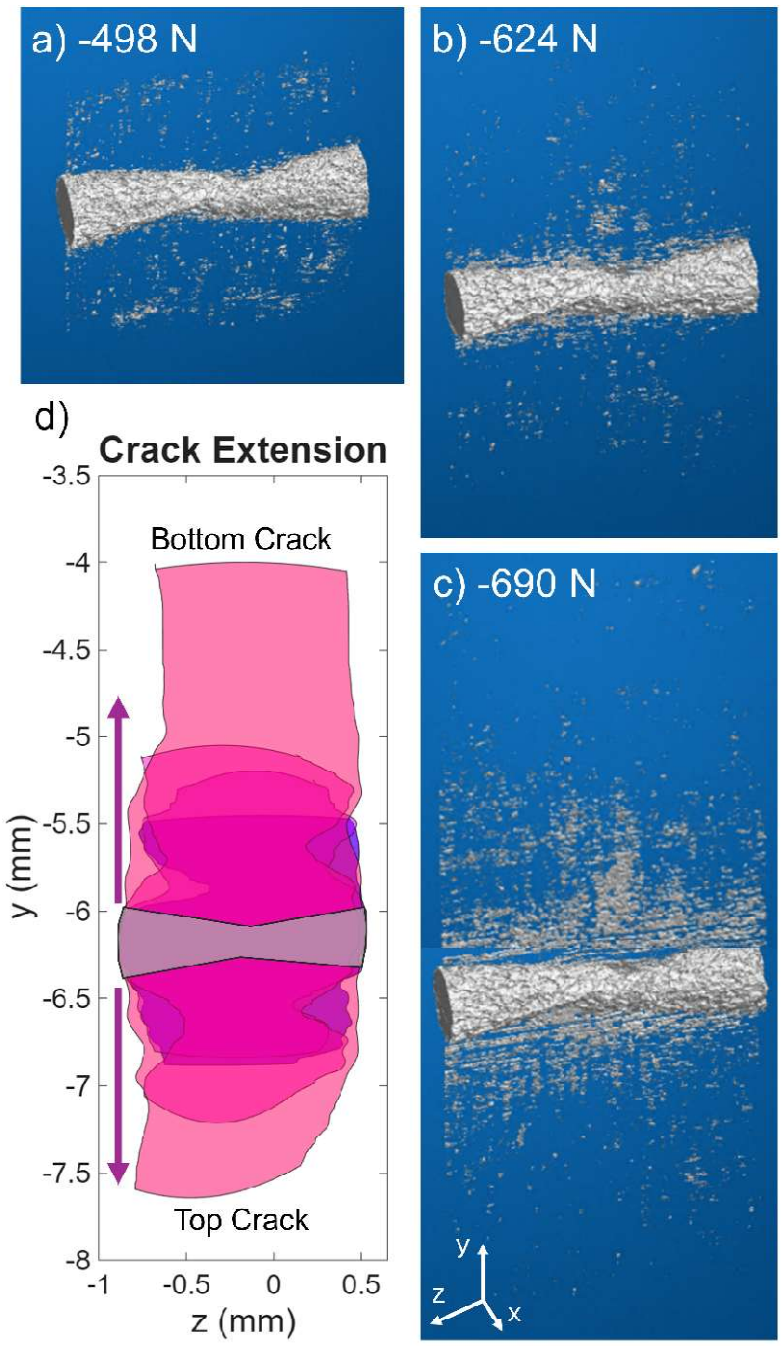

Figure 3.3: Crack extension in the TGC sample. a) Initial pop-in observed at -498 N. b) A regular extension event at -624 N. c) At -690 N, the top crack (more negative *y*) extended normally, while the bottom crack appeared to extend normally but underwent a secondary extension event and was eventually detected again deeper in the sample. d) All crack extensions overlaid, with darker colors corresponding to earlier extension events. The frame orientation is labeled in the bottom of c).

3.3.1.2 Fracture toughness

Using Equation 2.5 [18] with the load at extension and calculated crack lengths, the fracture toughness K_{Ic} can be calculated for all extensions for both the top and bottom cracks (Figure 3.4). Most values fall between 1.4 and 1.6 MPa√m. This range is similar to the fracture toughnesses of many other glass-ceramics with silicate-based matrices and low crystalline volume fractions studied in other experimental modes [19-22]. Additionally, the fracture toughness is higher than a pure glass, as expected [22,23]. Promisingly, the fact that these values correspond indicates that the DCDC experiments are successfully capturing crack extension similar to that seen in other experiments. Thus, the cracks described here are not irrelevant to fracture in other geometries and models or simply academic in nature.

The highest recorded fracture toughness corresponds to the top crack at -523 N, at which load the bottom crack extended but the top did not, resulting in its length being the same as the previous calculation. The fracture toughness is not reported for the final extension in the bottom crack, as the initial extension length was not obtained before the secondary extension event, and the extension which was recorded occurred in a volume where the cross-sectional area changed with depth, meaning a single stress value is invalid.

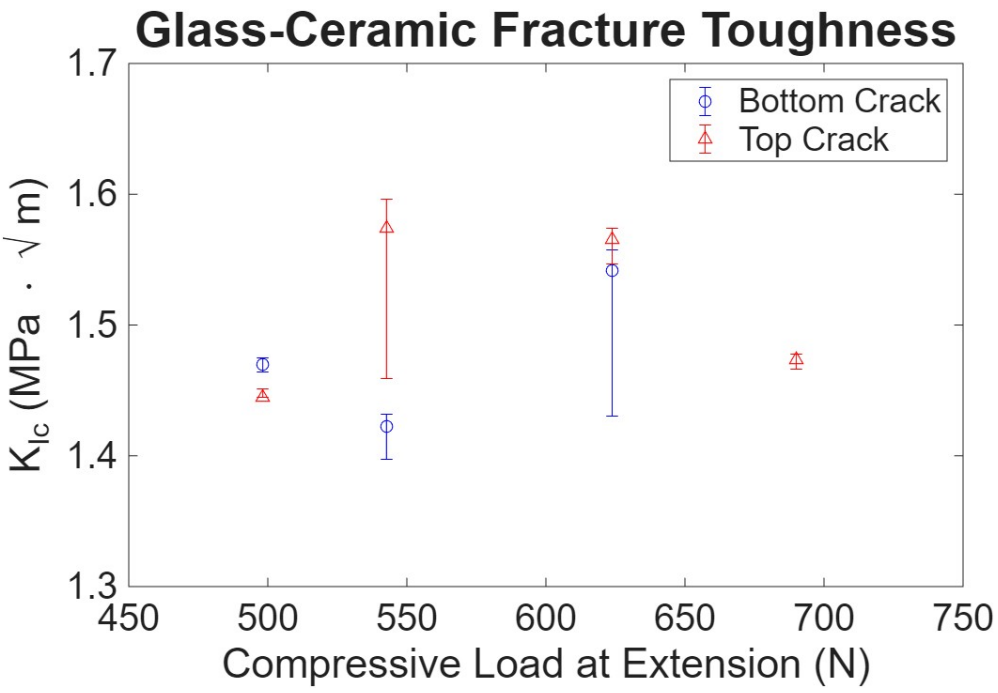

Figure 3.4: Fracture toughness in the DCDC TGC sample using Equation 2.5 [18].

3.3.2 Trevorite grain response

3.3.2.1 Stress response

Near-zero load analysis of the FF-HEDM results for the trevorite grains reveals a wide distribution of strains, and therefore stresses. Given the thermal history of the TGC sample and the mismatch in properties between the trevorite grains and the silicate matrix, residual stress is expected in the trevorite crystals, which have a larger thermal expansion coefficient than a typical glass.

The Selsing model (Equation 3.1) can be used to estimate residual stresses in a model glass ceramic system with evenly distributed, spherical, isotropic crystals in a volume fraction smaller than 10% [3,24]. While more idealized than the reality of the TGC system, the cubic, equiaxed nature of the grains allows this model to be used as an initial estimate for the residual stresses present in the TGC sample before loading.

$$\sigma_T = \frac{\Delta\alpha \cdot \Delta T}{(1+\nu_M)/2E_M + (1-2\nu_T)/E_T} \qquad \text{Equation 3.1}$$

$\Delta\alpha$ = difference in thermal expansion coefficients

ΔT = difference between glass transition temperature and room temperature

ν = Poisson's Ratio

E = elastic modulus

Average values for the elastic constants and the thermal expansion coefficient of trevorite can be obtained from geological studies [13], while the matrix properties can be estimated from average properties of alkali-alumino-silicate glasses [23,25]. The glass-transition temperature of the glassy phase can be estimated from the liquidus temperature [8] and a simplified relationship (T_g/T_l = 2/3) between the two [26]. All values are reported in Table 3.1.

Table 3.1: Estimated properties of trevorite and the silicate matrix for use in Equation 3.1.

	Matrix	Trevorite
Elastic modulus E	70 GPa	183 GPa
Poisson's ratio ν	0.25	0.33
Thermal expansion coefficient α	60×10^{-7} °C $^{-1}$	25.8×10^{-6} °C $^{-1}$
Glass-transition temperature T_g	—	780 °C

The resultant estimated residual stress in the trevorite particles is 1386 MPa. Since these particles are not pure trevorite but likely have many substitutions [27], and since they are anisotropic, are not perfectly spherical, and have a range of sizes, the crystals had a spread

in stress, especially as load was applied, and the average could also vary from this value. However, since the true value of the unstrained lattice parameter is unknown for this specific formulation, it has been set to a value of 8.36 Å, for which the average stress in the trevorite crystals across all of the *x*, *y*, and *z* directions was 1465 MPa and nearly all stresses in all directions were tensile in nature (Figure 3.5). This lattice parameter represents an increase of 0.25% from the nominal unstrained lattice parameter of 8.339 Å [13].

While the load in the matrix is unknown due to FF-HEDM not providing data on amorphous materials, the radial stress around glass-ceramic particles with residual stress is known to be related to the stress in the particles, dropping off as r^{-3} with distance from each particle [3].

The FF-HEDM results for the stress and strain in the trevorite crystals at the different loads for which data were collected are presented as raincloud plots in Figure 3.5. While the stresses in all directions had similar values at near-zero load, the stresses in the *y* direction decreased with applied load (Figure 3.5a-b), indicating they took on some of the overall compressive stress on the sample, while the stresses in *x* and *z* increased slightly in accordance with expected transverse stresses for samples under compressive load (Figure 3.5c-f). While most of the grains had values clustered around the averages in each direction, indicated by the width of the quartiles in the box plots and the shape of the histograms, there were a number of outliers both with greater and lesser magnitude in both stress and strain at all loads in all directions.

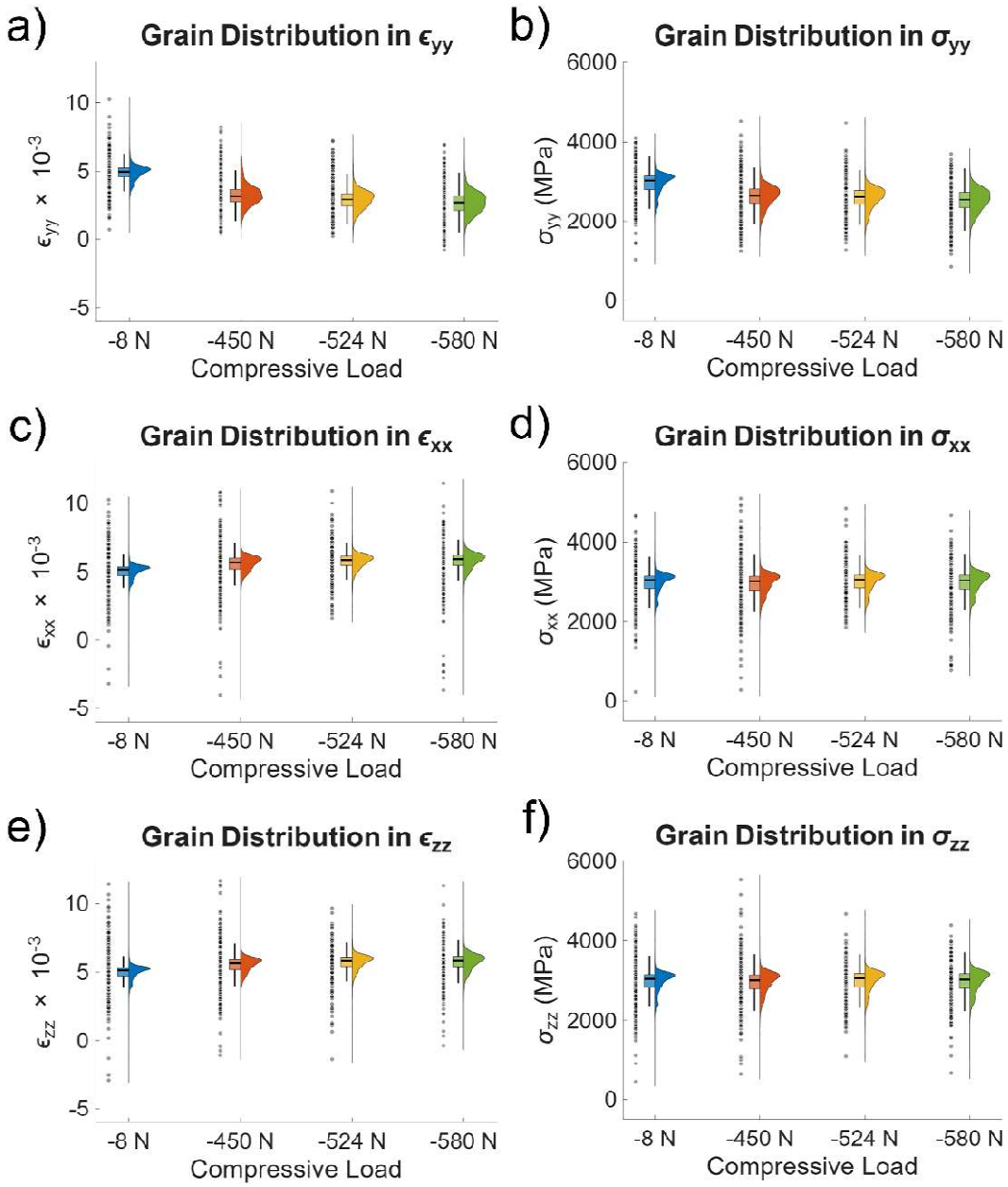

Figure 3.5: Strains and stresses in the trevorite crystals in the TGC sample, depicted as rainclouds plots. For each set of data collected, the data points are plotted on the left, a boxplot showing the quartiles and median value of each dataset is presented in the center, and a histogram is plotted on the right showing the relative frequencies of values. a-b) Strain and stress in the loading (*y*) direction, respectively, showing a decrease in average value with load. c-d) Strain and stress in the *x* direction, oriented perpendicular to the hole axis. e-f) Strain and stress in the *z* direction, oriented along the hole axis.

While the overall stresses are informative for demonstrating that the trevorite crystals, and not just the matrix, were impacted by the overall applied load on the sample, stress is additionally known to be impacted by the crack front, as a Mode I crack in the DCDC geometry has a tensile region ahead of the crack tip working to open it upon an increase in load. As the FF-HEDM scans were collected near the estimated crack front, the stresses at a given load can be subdivided into smaller volumes and analyzed. Figure 3.6 depicts the average stresses in each 0.25 mm-tall volume as a function of distance for the crack, for datasets collected at both the top and bottom crack front at two different loads. The grains near the crack, that is, directly above or below any part of the hole, are differentiated from those in the rest of the sample bulk.

For all datasets except for that of the top crack front at -450 N (Figure 3.6a-b), the stress values for grains near the crack plane were more tensile than those in the sample bulk in both the *x* and *y* directions until a distance of about 0.3 mm away from the crack tip, when the two populations coincided. Notably, the early top crack with the lowered stress values, after popping-in at -498 N, did not extend until a load of -624 N was reached, compared to the extension at -523 N experienced by the bottom crack (Figure 3.6d). Despite similar pop-in lengths, the increase in tensile stress as a result of the crack was suppressed for the top crack, with the populations ahead of and away from the crack having similar values, in contrast to the bottom half of the sample, where grains ahead of the crack experienced more tensile stress (Figure 3.6c-d). The average values for σ_{xx} and σ_{yy} for all grains in the top half of the sample at that load were also on average lower than those at similar distances from the crack in the bottom half of the sample, indicating a greater sample resistance to cracking in that region. When the top crack did extend, it moved about 0.3 mm further into the sample, stopping before a region with a large increase in σ_{yy} for both populations (Figure 3.6b) but a depression in σ_{xx} for the grains ahead of the crack (Figure 3.6a). While these trends may have changed somewhat at the higher load, the lowered tensile stress in that volume in the *x* direction indicates that higher loads were necessary to induce further tensile stress and to reach a sufficient crack-opening stress for propagation. As a result, the fracture toughness should be higher in that region than in the opposing crack.

At -580 N, the stresses in the crack plane were greater in magnitude than those in the sample bulk in both *x* and *y* at nearly all distances, indicating the effect of the crack tip on

the region (Figure 3.6e-h). While both cracks extended during the next extension event, the bottom crack experienced the secondary extension discussed in Section 3.3.1.1 and grew to a greater length. Similarly to the grains at -450 N, the stresses in both *x* and *y* for the crack which grew longer (Figure 3.6g-h) were higher on average than those near the crack which grew to a shorter length (Figure 3.6e-f), again indicating a reduction in resistance to the crack for regions with higher tensile stresses, where less applied load was required to exceed the stresses required for crack extension, decreasing fracture toughness.

The difference in local average stresses and fracture toughness could be a result of several different factors. During quenching, the sample cooled faster in some regions than in others, likely causing a difference in residual stress, and therefore in the stress field encountered by the crack. Additionally, due to the number of oxides present in the initial melt which can substitute into the trevorite lattice, and the potential for uneven distribution of ions, the lattice parameter for each grain might vary, resulting in a different actual strain on the lattice than reported. Furthermore, while the grains are generally evenly distributed, there might be some volumes with a higher or lower average grain diameter, which also would affect the stress distribution.

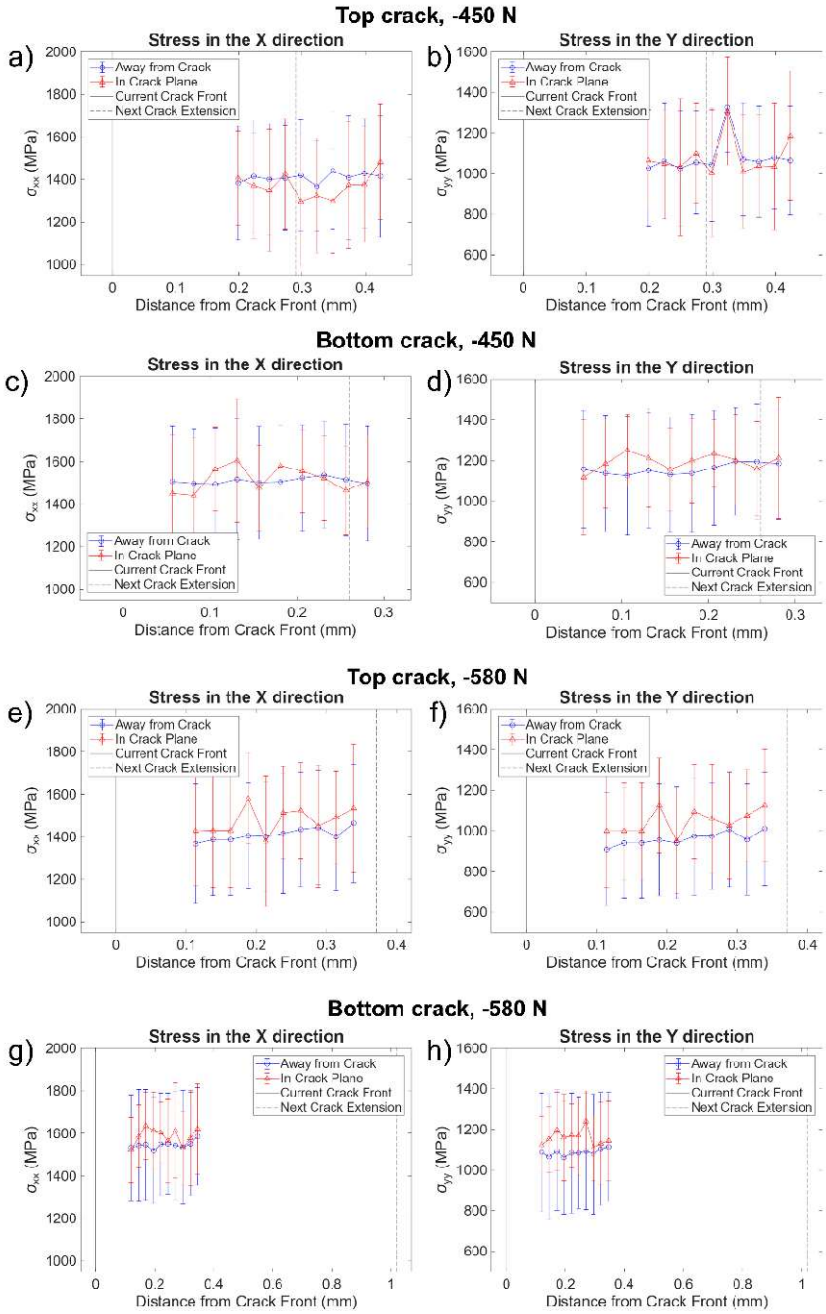

Figure 3.6: Stresses in the trevorite crystals with distance from the crack front, for both the top and bottom cracks at two different loading states. a-b) In the top crack at -450 N, which did not grow until -624 N, σ_{xx} and σ_{yy} for grains ahead of the crack are not larger than for grains away from the crack, and their values are depressed when compared to those in the bottom crack (c-d), which grew at -523 N. e-f) In the top crack at -580 N, the stresses are again on average lower than those on the bottom (g-h), which grew to a greater length in the next group of extension events.

3.3.2.2 Fracture response

For particles with a thermal expansion coefficient greater than that of the matrix, a growing crack will be deflected away from the particles rather than attracted to them [5,7]. Thus, the crack is expected to diverge away from the trevorite particles in the TGC system. This was indeed the case for most of the particles in the studied sample; however, certain particles were also cracked through in a transgranular manner, and others appeared to bridge the crack, at least partially. The three types of particle-crack interaction are shown in a tomography slice in Figure 3.7a, along with the same slice before the crack propagated (Figure 3.7b) to verify transgranularity. Grains which deflected the crack will be termed intergranular henceforth for ease of description and comparison, although this type of crack is really inter-granular-matrix rather than truly existing between two grains on a grain boundary.

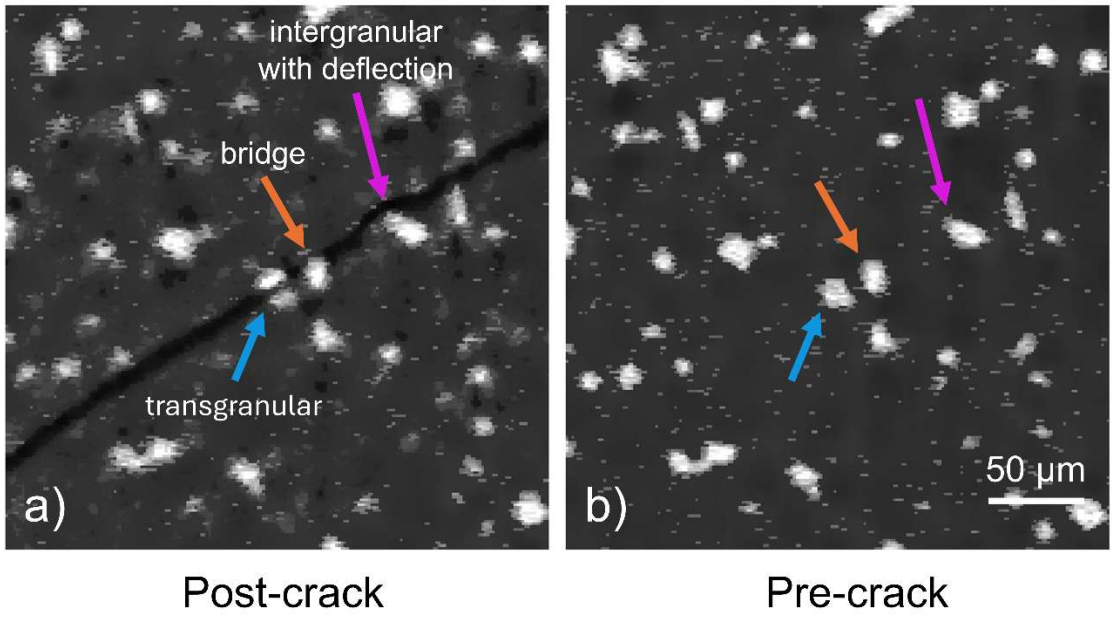

Figure 3.7: Types of grains which interacted with the crack. a) A tomographic slice showing transgranular grain, a grain which bridged the crack, and an intergranular grain, which the crack had to deflect to go around. b) The same slice from before the crack propagated, verifying that the transgranular grain was originally a single grain.

The different populations of grains can be examined to determine what factors led to them cracking in the manner that they did. Figure 3.8 shows FF-HEDM data for orientation

and mechanical state collected at near-zero load for the grains in the 500-μm tall volume around the hole to examine whether any of these properties is predictive for whether the crack propagated through or around a grain.

Figure 3.8a shows the orientation of the grains projected along the *y*-direction, along which the crack propagated, and thus the planes perpendicular to it. The orientations for all grains in the volume are shown to emphasize the random nature of grain orientation. Intergranular, transgranular, and bridging grains are highlighted, with all the populations mixed. While the crack does seem not to have moved transgranularly through grains with a near-<100> normal, nor did grains with a near-<111> normal, grains which the crack was deflected around occupy orientations across the fundamental region, limiting those traits in being predictive factors for crack motion. Figure 3.8b then shows the orientation of lattice planes on which the crack moved transgranularly, or did not move, either by deflection or by bridging. Again, there is little trend for any one population to explain why a crack might move onto or avoid a particular plane; the absence of data points near the {100} directions belonging to any of the populations simply indicates a lack of encounters on that plane family, since it did not move to or avoid those planes.

Next, Figure 3.8c shows the granular strain, in the *x* (crack opening) and *y* (loading) directions, while Figure 3.8d displays stress in the same directions. The other grains in the region of the crack (above or below the hole) are also shown. Once again, the populations are mixed in with one another as well as the overall population, and the presence of outliers only serves to show that a particular value or ratio of values is not sufficient to predict the way a crack will grow as it nears a grain.

This makes sense, as from a purely theoretical standpoint, all the grains, regardless of orientation, should lead to crack deflection. Even though they did display a range of residual stresses at near-zero load, those stresses were still tensile in nature, indicating the assumptions made about their properties in comparison to the matrix are reasonable, and again, should lead to crack deflection. Thus, additional factors resulting from the arrangement of grains in the sample, the grain or sample geometry, or other experimental conditions must be affecting the crack.

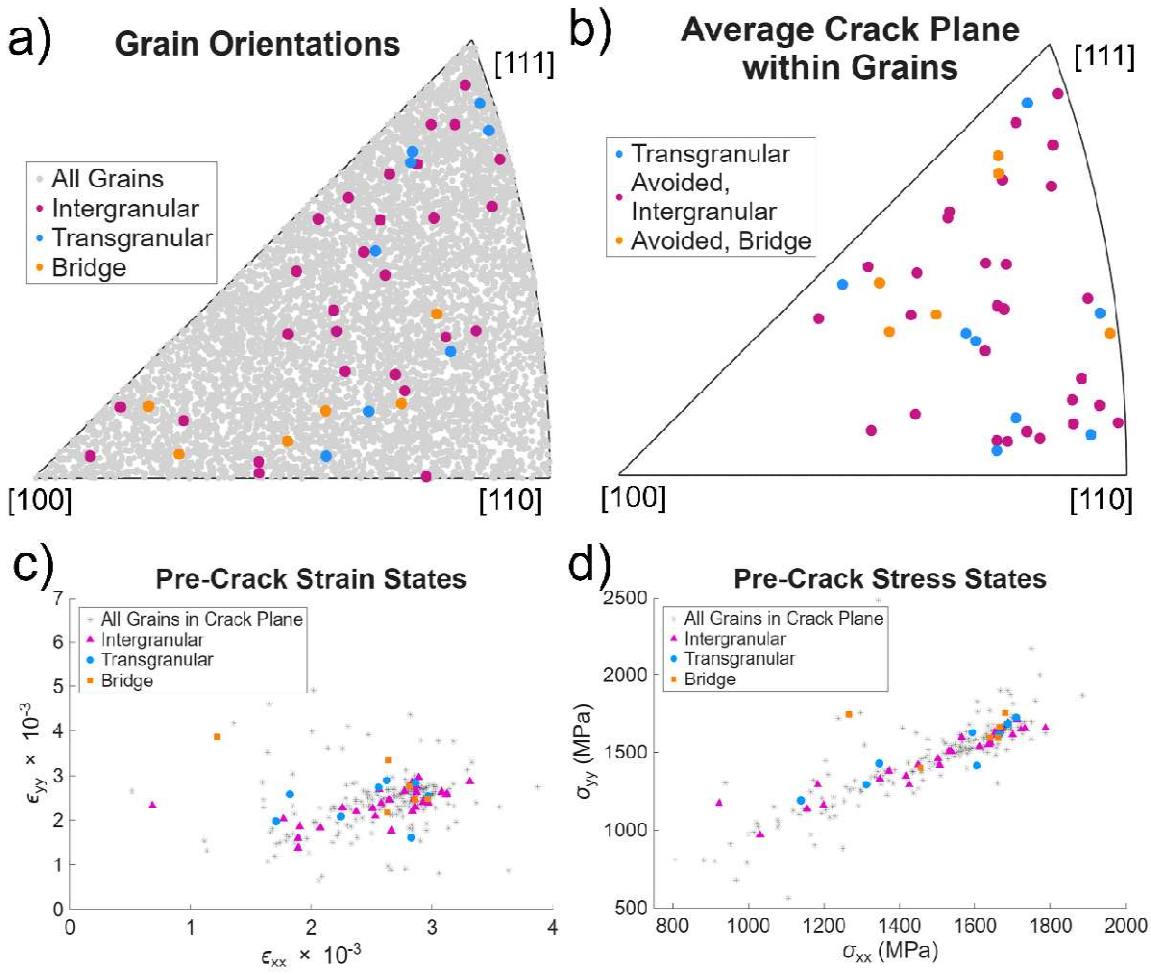

Figure 3.8: FF-HEDM data for intergranular, transgranular, and bridging grain populations at near-zero load. a) The orientation of the lattice planes perpendicular to the crack's direction of motion. While the transgranular and bridging grains show some trend, intergranular grains overlap with those values. b) The orientation of the lattice plane on which transgranular cracks moved, along with the orientation of the crack if it had not been deflected in intergranular grains or stopped by bridging grains. c-d) Strain and stress states, respectively, in the *x* (crack opening) and *y* (loading) directions, for grains of the three populations compared to all grains in the crack plane.

3.3.2.3 Crack deflection

In the absence of any predictive quality in the grains themselves, the relation between the crack and the grains is of potential use. Fracture toughness is related to the strain field, which itself is related to angle relative to the crack tip [5,28]. Thus, while a deflection may

lead the crack to grow in a more favorable location than through a grain with high fracture toughness and residual stress, it can also be true that a deflection may be less favorable than the transgranular crack at certain angles. Figure 3.9a shows the angles of deflection for grains which did deflect the crack, as well as the theoretical angles at which it would have had to deflect to go around the grains it ultimately passed through transgranularly or which it bypassed entirely, leading to a bridge. The method of angle calculation was to average the absolute values of the deflection angle at the grain's maximum cross-section to the nearby straight section of the crack. Figure 3.9b reproduces the tomography slices of Figure 3.7a with angles labeled. The transgranular and bridging grain are at their maximum cross sectional area, while the intergranular grain is not; at its maximum area, its facets coincided with the labeled angles. From Figure 3.9a, the crack moves intergranularly when the angle of deflection, averaged from the absolute values on either side of the grain, is less than about 0.45 radians, or 25.8°. Required deflections greater than that value are avoided, with the crack moving straight through the impinging grain instead. Greater deflections usually coincide with larger grains, which more regularly cross over the central crack plane (Figure 3.9c), but are also dependent on the centroids being close to the average crack plane, such that large grains located about one radius away from the crack plane can still crack intergranularly. Figure 3.9c also shows that the angle of deflection is not dependent on grain orientation; instead, it is mainly impacted by the grain geometry.

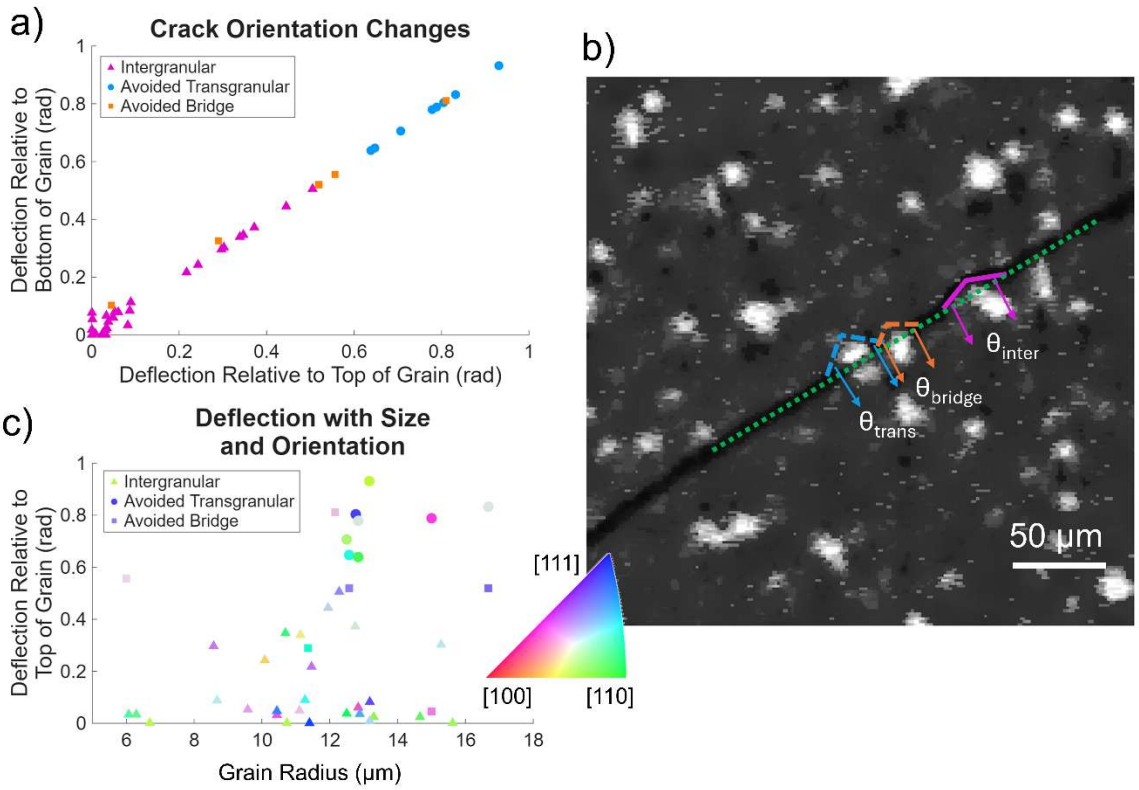

Figure 3.9: Crack deflection and grain type. a) Intergranular grains deflect the crack up to a maximum of 0.45 radians, while the crack would have to theoretically deflect at larger angles to go around grains which eventually cracked transgranularly or acted as bridges. b) The tomographic slice of Figure 3.7a reproduces with deflection angles labeled. c) Deflection angle as a function of grain radius and colored by the orientation of Figure 3.8a in standard inverse pole figure colors (inset).

A point of note in Figure 3.9a is that there are two grains which bridged the crack with angles smaller than 0.45 radians. Figure 3.10 shows these grains in detail, demonstrating that both have a high aspect ratio in contrast to the mostly equiaxed grains in the majority of the sample. Figure 3.10a-e shows the grain with the theoretical deflection of about 0.25 radians in successive slices spaced 3 μm apart, showing that the visible edge was oriented roughly parallel to the crack. The grain was tilted in the *y* direction, causing the cross-section to move across the crack plane with increasing depth. While the crack could move intergranularly around one side, the deflection to continue around it would increase as the cross-section moved away from the crack plane. As a result, the crack actually moved intergranularly when one of the faces coincided with the crack plane (Figure 3.10a,e), but moved transgranularly

in the center of the grain, with minimal deflection (Figure 3.10c). At intermediate stages, as the crack transitioned to transgranular and back, it bridged the crack (Figure 3.10b,d).

The other bridging grain, with a theoretical deflection of less than 0.1 radians, also had a high aspect ratio, but was oriented perpendicular to the crack plane (Figure 3.10f), acting like a reinforcing fiber working to hold the sample together, which has been observed in other glass-ceramics with high aspect ratio crystals, such as lithium disilicate-based glass-ceramics [29,30].

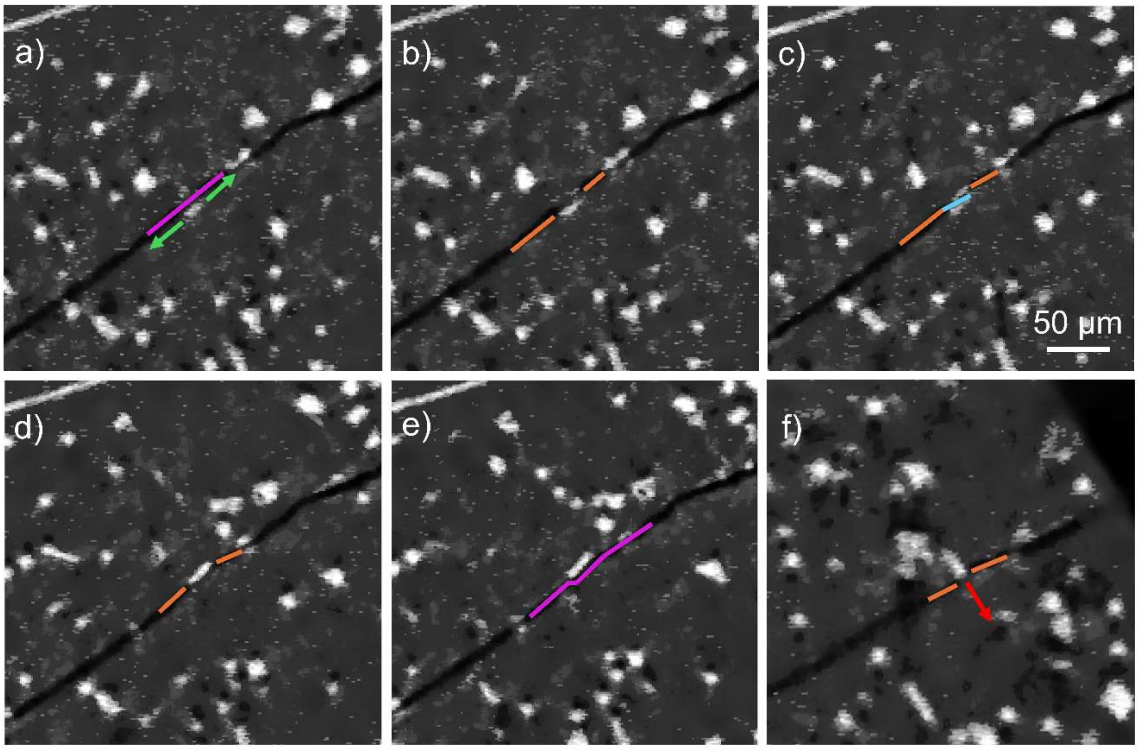

Figure 3.10: Two high aspect ratio grains bridging the crack in different ways. a-e) A grain oriented parallel to the crack plane, that transitions from intergranular cracking, through bridging, to transgranular cracking, and back again at different crack depths. f) A grain oriented perpendicular to the crack plane, acting as a reinforcing fiber.

Intergranularly-cracked grains with relatively large (>0.4 radians) deflection angles can also be considered. Notably, for one such grain, it is found to be directly opposite two different, smaller grains located at different depths, both of which have a smaller deflection angle (Figure 3.11b,c). The crack moves between these two grains in true intergranular fashion, with the smaller deflection around the two smaller grains serving as a favorable

cracking location offsetting any potential hindrance by the larger deflection around the larger grain.

Figure 3.11 also demonstrates the tendency of the crack to remain straight in the absence of grains, a phenomenon seen in other materials primarily cracking in a Mode I fashion [16]. Figure 3.11a shows the crack 6 μm before the appearance of the top face of the large grain in Figure 3.11b,c), where it is nearly entirely straight. In Figure 3.11d, 6 μm deeper along the crack beyond the large grain's bottom face, the deflection has almost straightened out again, demonstrating its tendency to return to straight in the isotropic matrix, where there are no lattice planes on which for it to persist or facets around which it deflects.

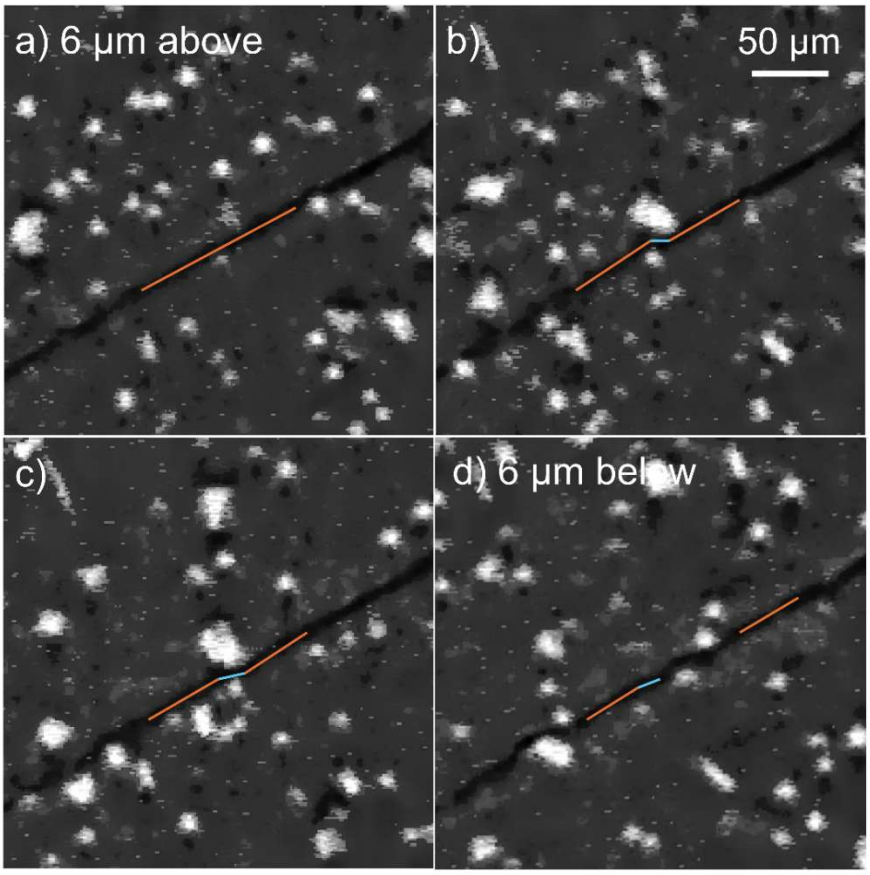

Figure 3.11: Crack deflection as a function of sample depth. a) Closer to the hole and 6 μm above the top edge of the large grain in b) and c), the crack is straight in the absence of local grains. b) The crack deflects between two grains. c) The large grain above the crack is the same as in b) while the smaller one below is a different grain located underneath the small grain in b), and the crack has continued to deflect. d) 6 μm below the bottom edge of the large grain in b) and c), the kink remaining from the deflection has almost straightened out.

3.4 Conclusion

The system of synchrotron X-ray HEDM and μ-CT is demonstrated to work admirably to reveal both the crack and the microstructure in the TGC sample. By combining the stable fracture of the DCDC geometry and the precise loading of RAMS-II, we were able to induce, grow, and pause cracks in the sample, allowing for investigation of the microstructure and the crack shape at multiple loading iterations. General expectations for the glass-ceramic were met, with the higher thermal expansivity of the trevorite grains compared to the matrix creating residual stresses that tended to deflect the crack, but only at deflection angles smaller than 0.45 radians. As a result, crack bridging, especially by grains of high aspect ratio, and transgranular cracking were also observed, dependent largely on deflection angle. The number of observations of different types of cracking should serve as useful information for modelers seeking to verify their work and to incorporate multiple material responses into their models.

Additionally, stress variations in grains ahead of the crack were revealed using FF-HEDM. Two cracks in the same sample of about the same length may grow at different loads and to different lengths upon application of load based on the accumulation of local stresses, with higher tensile stresses ahead of the crack before propagation leading to a lowered fracture toughness as less load is needed to reach the critical point for crack extension.

Further investigation into glass-ceramics with non-cubic crystalline phases and higher aspect ratios would serve as a useful extension to this work and to future, more advanced models, especially with the results regarding crack bridging. In particular, lithium disilicate-based glass-ceramics are broadly used in many applications [1,2], making such results highly relevant, and the behavior of the lenticular crystalline phase would present a different set of insights to those presented here that could help elucidate key similarities and differences between different classes of glass-ceramics and dual-phase systems.

Acknowledgments

This work was sponsored by the US Office of Naval Research Grant No. N00014-21-1-2784. SFG was also supported by the US National Science Foundation Graduate Research Fellowship No. 2139433. Additionally, the authors would like to thank Dr. Paul Shade and the Air Force Research Laboratory for the generous use of RAMS2. This work

is based on research conducted at the Center for High-Energy X-ray Sciences (CHEXS), which is supported by the National Science Foundation (BIO, ENG and MPS Directorates) under award DMR-2342336.

Bibliography

[1] Y. Jiang, C. Zhang, J. Xu, J. Xu, X.-Q. Zhan, N. Ma, F.-C. Tsai, An overview of dental glass–ceramics: From material design to the manufacturing process, *Int J Ceram Eng Sci* 6 (2024) e10224. https://doi.org/10.1002/ces2.10224.
[2] G.H. Beall, Design and properties of glass-ceramics, *Annu Rev Mater Sci* 22 (1992) 91–119. https://doi.org/10.1146/annurev.ms.22.080192.000515.
[3] F.C. Serbena, E.D. Zanotto, Internal residual stresses in glass-ceramics: A review, *J Non-Cryst Solids* 358 (2012) 975–984. https://doi.org/10.1016/j.jnoncrysol.2012.01.040.
[4] A.G. Evans, Microfracture from thermal expansion anisotropy—I. Single phase systems, *Acta Metall* 26 (1978) 1845–1853. https://doi.org/10.1016/0001-6160(78)90097-4.
[5] K.T. Faber, A.G. Evans, Crack deflection processes—I. Theory, *Acta Metall* 31 (1983) 565–576. https://doi.org/10.1016/0001-6160(83)90046-9.
[6] K.T. Faber, A.G. Evans, Crack deflection processes—II. Experiment, *Acta Metall* 31 (1983) 577–584. https://doi.org/10.1016/0001-6160(83)90047-0.
[7] R.W. Davidge, T.J. Green, The strength of two-phase ceramic/glass materials, *J Mater Sc*i 3 (1968) 629–634. https://doi.org/10.1007/BF00757910.
[8] C.E. Lonergan, J. Rice, C. Skidmore, M.J. Schweiger, P. Hrma, The effects of mixing multi-component HLW glasses on spinel crystal size, *J Nucl Mater* 558 (2022) 153318. https://doi.org/10.1016/j.jnucmat.2021.153318.
[9] J.N. Cuzzi, D.M. Olson, Recovering 3D particle size distributions from 2D sections, *Meteorit Planet Sci* 52 (2017) 532–545. https://doi.org/10.1111/maps.12812.
[10] P.A. Shade, B. Blank, J.C. Schuren, T.J. Turner, P. Kenesei, K. Goetze, R.M. Suter, J.V. Bernier, S.F. Li, J. Lind, U. Lienert, J. Almer, A rotational and axial motion system load frame insert for in situ high energy x-ray studies, *Rev Sci Instrum* 86 (2015) 093902. https://doi.org/10.1063/1.4927855.
[11] K.E. Nygren, D.C. Pagan, J.V. Bernier, M.P. Miller, An algorithm for resolving intragranular orientation fields using coupled far-field and near-field high energy X-ray diffraction microscopy, *Mater Charact* 165 (2020) 110366. https://doi.org/10.1016/j.matchar.2020.110366.
[12] J. Bernier, P. Avery, S. Soderlind, D. Boyce, B. Major, S. Zack, K. Nygren, P. Shade, HEXRD/hexrd: Release 0.9.6, (2024). https://doi.org/10.5281/zenodo.12095606.
[13] R.C. Liebermann, Pressure and temperature dependence of the elastic properties of polycrystalline trevorite (NiFe2O4), *Phys Earth Planet In* 6 (1972) 360–365. https://doi.org/10.1016/0031-9201(72)90059-3.
[14] Chess Analysis Pipeline (CHAP) — CHESS Analysis Pipeline, (n.d.). https://chesscomputing.github.io/ChessAnalysisPipeline/ (accessed April 15, 2026).

[15] J.K. Kurihara, T. Tomimatsu, Y.F. Liu, S.Q. Guo, Y. Kagawa, Mode I fracture toughness of SiC particle-dispersed ZrB2 matrix composite measured using DCDC specimen, *Ceram Int* 36 (2010) 381–384. https://doi.org/10.1016/j.ceramint.2009.07.031.
[16] B. Cotterell, On brittle fracture paths, *Int J Fract* 1 (1965) 96–103. https://doi.org/10.1007/BF00186747.
[17] T. Fett, G. Rizzi, J.P. Guin, J.M. López-Cepero, S.M. Wiederhorn, A fracture mechanics analysis of the double cleavage drilled compression test specimen, *Eng Fract Mech* 76 (2009) 921–934. https://doi.org/10.1016/j.engfracmech.2008.12.016.
[18] Q.Z. Wang, M. Ni, L.Z. Wu, R.Q. Huang, Scrutinized and revised stress intensity factor formulas for double cleavage drilled compression specimens, *Theor Appl Fract Mec* 96 (2018) 803–810. https://doi.org/10.1016/j.tafmec.2017.11.008.
[19] L. Sant'Ana Gallo, F. Célarié, J. Bettini, A.C.M. Rodrigues, T. Rouxel, E.D. Zanotto, Fracture toughness and hardness of transparent MgO–Al2O3–SiO2 glass-ceramics, *Ceram Int* 48 (2022) 9906–9917. https://doi.org/10.1016/j.ceramint.2021.12.195.
[20] B. Deng, J. Luo, J.T. Harris, C.M. Smith, M.E. McKenzie, Molecular dynamics simulations on fracture toughness of Al2O3-SiO2 glass-ceramics, *Scripta Mater* (2019) 277–280. https://doi.org/10.1016/j.scriptamat.2018.11.034.
[21] K.S. Jodha, N. Kaur, S.M. Salazar Marocho, J.J. Mecholsky, S.T. Lirette, Y. Duan, J.A. Griggs, Relationship between fracture toughness and fractal dimensional increment in two types of dental glass-ceramics with different fracture surface roughness, *Dent Mater* 38 (2022) 1977–1988. https://doi.org/10.1016/j.dental.2022.11.011.
[22] M. Tiegel, R. Hosseinabadi, S. Kuhn, A. Herrmann, C. Rüssel, Young's modulus, Vickers hardness and indentation fracture toughness of alumino silicate glasses, *Ceram Int* 41 (2015) 7267–7275. https://doi.org/10.1016/j.ceramint.2015.01.144.
[23] T. Rouxel, S. Yoshida, The fracture toughness of inorganic glasses, *J Amer Ceram Int* 100 (2017) 4374–4396. https://doi.org/10.1111/jace.15108.
[24] J. Selsing, Internal Stresses in Ceramics, *J Amer Ceram Int* 44 (1961) 419–419. https://doi.org/10.1111/j.1151-2916.1961.tb15475.x.
[25] S.M. Salman, S.N. Salama, Thermal expansion data of some alkali aluminosilicate glasses and their respective glass-ceramics, *Thermochim Acta* 90 (1985) 261–276. https://doi.org/10.1016/0040-6031(85)87104-5.
[26] S. Sakka, J.D. Mackenzie, Relation between apparent glass transition temperature and liquids temperature for inorganic glasses, *J Non-Cryst Solids* 6 (1971) 145–162. https://doi.org/10.1016/0022-3093(71)90053-6.
[27]S.A. de Waal, Nickel minerals from Barberton, South Africa: V. trevorite, redescribed, *Am Mineral* 57 (1972) 1524–1527.
[28] Continuum aspects of crack propagation I: linear elastic crack-tip field, in: Fracture of Brittle Solids, 2nd ed., Cambridge University Press, Cambridge, 1993: pp. 16–50. https://doi.org/10.1017/CBO9780511623127.
[29] K. Suputtamongkol, K.J. Anusavice, J.J. Mecholsky, Cyclic contact fatigue behavior of baria-silicate glass-ceramics as a function of crystal aspect ratio, *J Eur Ceram Soc* 42 (2022) 2441–2448. https://doi.org/10.1016/j.jeurceramsoc.2022.01.012.
[30] E. Apel, J. Deubener, A. Bernard, M. Höland, R. Müller, H. Kappert, V. Rheinberger, W. Höland, Phenomena and mechanisms of crack propagation in glass-ceramics, *J Mech Behav Biomed* 1 (2008) 313–325. https://doi.org/10.1016/j.jmbbm.2007.11.005.